frontiers | Frontiers in Physics

TYPE Original Research
PUBLISHED 18 November 2025
DOI 10.3389/fphy.2025.1644477

OPEN ACCESS

EDITED BY
Muriel Fallot,
UMR6457 Laboratoire de Physique Subatomique et des Technologies Associées (SUBATECH), France

REVIEWED BY
Zhuang Ge,
University of Jyväskylä, Finland
Ana Isabel Morales López,
University of Valencia, Spain

*CORRESPONDENCE
W. Xian,
xianwd5@mail.sysu.edu.cn
M. Rosenbusch,
marco.rosenbusch@riken.jp
V. H. Phong,
phong@ribf.riken.jp

†PRESENT ADDRESS
M. Wada,
Institute of Modern Physics, Chinese Academy of Sciences, Lanzhou, China
S. Chen,
School of Physics, Engineering and Technology, University of York, York, United Kingdom

‡Deceased

RECEIVED 10 June 2025
REVISED 06 August 2025
ACCEPTED 18 September 2025
PUBLISHED 18 November 2025

CITATION
Xian W, Rosenbusch M, Phong VH, Wada M, Schury P, Hou D, Takamine A, Chen S, Niwase T, Hirayama Y, Ishiyama H, Iimura S, Ito Y, Kojima TM, Kimura S, Liu J, Lee J, Michimasa S, Miyatake H, Moon JY, Mukai M, Nishimura S, Naimi S, Sonoda T, Watanabe YX, Wollnik H and Yan S (2025) Atomic mass measurements of neutron-rich nuclides on the path to ^{78}Ni with a β-TOF-equipped MRTOF device.
Front. Phys. 13:1644477.
doi: 10.3389/fphy.2025.1644477

Atomic mass measurements of neutron-rich nuclides on the path to ^{78}Ni with a β-TOF-equipped MRTOF device

W. Xian[1,2,3]*, M. Rosenbusch[4]*, V. H. Phong[4]*, M. Wada[3†], P. Schury[3], D. Hou[5], A. Takamine[4,6], S. Chen[2,3†], T. Niwase[3,4,6], Y. Hirayama[3], H. Ishiyama[4], S. Iimura[4], Y. Ito[3,7], T. M. Kojima[4], S. Kimura[4], J. Liu[2], J. Lee[2], S. Michimasa[8], H. Miyatake[3], J. Y. Moon[9], M. Mukai[3,4], S. Nishimura[4], S. Naimi[4,10], T. Sonoda[4], Y. X. Watanabe[3], H. Wollnik[11‡] and S. Yan[12]

[1]Sino-French Institute of Nuclear Engineering and Technology, Sun Yat-sen University, Zhuhai, China, [2]Department of Physics, The University of Hong Kong, Hong Kong SAR, China, [3]Wako Nuclear Science Center (WNSC), Institute of Particle and Nuclear Studies (IPNS), High Energy Accelerator Research Organization (KEK), Wako, Japan, [4]Institute of Physical and Chemical Research, Nishina Center for Accelerator-Based Science, Wako, Japan, [5]Institute of Modern Physics, Chinese Academy of Sciences, Lanzhou, China, [6]Department of Physics, Kyushu University, Fukuoka, Japan, [7]Advanced Science Research Center, Japan Atomic Energy Agency, Ibaraki, Japan, [8]Center of Nuclear Study (CNS), The University of Tokyo, Tokyo, Japan, [9]Institute for Basic Science, Daejeon, Republic of Korea, [10]Université Paris-Saclay, The French National Center for Scientific Research/National Institute of Nuclear and Particle Physics, Laboratoire de Physique des 2 Infinis Irène Joliot-Curie, Orsay, France, [11]Department of Chemistry and Biochemistry, New Mexico State University, Las Cruces, NM, United States, [12]Institute of Mass Spectrometry and Atmospheric Environment, Jinan University, Guangzhou, China

We report atomic mass measurements of the unstable nuclides $^{73–75}$Ni, $^{73–78}$Cu, and $^{74–78}$Zn, which have been accomplished using multi-reflection time-of-flight mass spectrometry combined with new technical developments to resolve challenges for exotic-isotope identification and selection. The isotopes were produced in-flight at the RIKEN's Radioactive Ion Beam Facility and delivered to the combined gas cell and multi-reflection system installed downstream of the ZeroDegree spectrometer. The incoming high-energy beam was energy-degraded and subsequently stopped in a helium gas cell. The energy degrader thickness was optimized using a new method that employs signals from plastic scintillators located upstream and downstream of the helium-filled gas cell. Extracted isotopes of interest were mass-selected by the in-MRTOF deflector method, for which we discuss simultaneous selection of multiple isobar chains. The ions of interest were identified unambiguously using β-decay-correlated mass measurements for the first time, which is demonstrated for ^{78}Zn. The new mass values are compared with literature values and recent measurements performed at JYFLTRAP and ISOLTRAP, where a generally good agreement is observed.

KEYWORDS

MRTOF-MS, β-TOF detector, in-MRTOF deflector, digital data acquisition system, r-process, coincidence measurement, neutron-rich exotic nuclei, neutron-capture cross sections

1 Introduction

Reaching the isotope ^{78}Ni has been one of the major goals for high-precision atomic mass measurements since its first production in 1995 [1]. A worldwide effort has since been spent to reach more neutron-rich Ni isotopes, where the physical interest is, in principle, two-fold. The first point of interest is to benchmark fundamental nuclear theory exploiting the double closed-shell configuration of ^{78}Ni, where the proton- and neutron-separation energies along the neutron numbers crossing the line $N = 50$, and the spectrum of excited states, have been investigated using advanced methods and interaction types [2–6]. In the last decades, there have been arguments about whether ^{78}Ni can preserve the doubly-magic character against the deformation, as the large neutron excess pairing correlations and cross-shell excitations (causing collective behavior) may lead to a decrease of the proton shell gap [7, 8]. Available experimental data to date suggests a stable configuration of the ^{78}Ni core [9–12], although multi-particle multi-hole excitations, core polarization, and intruder states have been highlighted in this region of the nuclear chart [13–15]. A second point of interest for isotopes in this vicinity comes from the importance in studies of stellar nucleosynthesis, where masses and half-lives are required for the estimation of neutron capture rates in hot stellar environments and, subsequently, in rapid neutron capture ("r-process") network calculations [16–19]. A further ingredient for astrophysical calculations, gaining recent interest, is the release of β-delayed neutrons, which causes a branching of the decaying nuclei towards stability [20].

While atomic masses of the Cu isotopes have been precisely measured up to $N = 50$ [11], and those of the Zn isotopes up to $N = 52$ [21], Ni isotopes have not yet been explored that far. When precise atomic mass measurements in the vicinity of the last two doubly-magic isotopes lacking precise atomic mass measurements – ^{78}Ni and ^{100}Sn – come into focus, low-energy mass measurements at radioactive ion beam (RIB) facilities are continuously reaching their limits. Beyond the limitations coming from the low production cross sections, the key challenges are ion-transport efficiency, ion selectivity, and being able to distinguish the ions of interest from background signals. The latter can come from real ionic background (contaminating ions), or from other sources like radioactive decay and dark counts at the ion detector. In ISOL-type facilities (*e.g.*, CERN/ISOLDE [22]), the extraction from the hot ISOL target depends on the ionization properties of the radioisotopes, and is thus element dependent. Furthermore, contaminating isobaric ions coming at high yields, *i.e.*, orders of magnitude higher than that of the wanted ions, demand the development of solutions to deal with such scenarios [21, 23, 24] for both Penning-trap (PTMS) [25–27] and multi-reflection time-of-flight (MRTOF) measurements [28–30].

In-flight facilities presently offer great promise due to higher production rates [31, 32]. Helium-gas filled stopping cells equipped with ion funnels or radiofrequency carpets (hereafter: radiofrequency gas cells, RFGC) build the energetic bridge between the high-energies of radioactive beams produced in-flight and the requirements for cooled ions in an ion trap [33–35]. Also at in-flight facilities both PTMS and MRTOF based high-precision mass measurements are being performed (see *e.g.*, [36, 37], and [29, 34, 38, 39]). Challenges for RFGC based experiments concern the stopping efficiency of the incoming ions, an efficient ion extraction from the RFGC, and the presence of abundant stable molecular ion contaminants; the latter becoming ionized by the beam and sometimes flooding the mass spectra with unwanted events. Additionally, chemical reactions with the incoming ions of interest can form radioactive molecules and distribute the valuable isotopes in molecular sidebands.

At the BigRIPS in-flight separator at RIKEN [31, 40, 41], an MRTOF mass spectrograph has been coupled to a 50 cm RFGC in through-beam configuration [42]. In the recent past, dedicated efforts have been spent to reach optimal stopping conditions of the incoming radioactive ions (RI) in a short time, to handle scenarios of unwanted molecule extraction from ionized contaminants in the He gas, and to reduce the background noise by decay-correlated ion identification. In this work, we describe and demonstrate the application of recent developments to resolve challenges under on-line conditions, with a focus on the first application of our β-TOF detector. At the same time, we will discuss the results of mass measurements for neutron-rich Ni isotopes and other isotopes in the vicinity, from two dedicated experiments (performed in 2020 and 2021). Among the results, we present high-precision mass measurements of ^{74,75}Ni, and compare the results with those from the JYFLTRAP group, recently published in [19].

2 Experimental procedure

In this section we briefly describe the experimental procedure. New developments and applications are described in detail in separate subsections.

To produce the radioactive ions (RI) of interest, primary beams of ^{238}U were accelerated to 345 MeV/u using a series of accelerators at the Radioactive Isotope Beam Factory (RIBF) [43] within RIKEN. The energetic primary beams impinged upon a 4 mm-thick ^{9}Be primary target, resulting in the production of a wide variety of RI – including those around ^{79}Cu – through in-flight fission reactions. The reaction products were accepted by the BigRIPS spectrometer [31, 40, 41] downstream of the target, where the desired RI were carefully selected, purified, identified, and then transported to the subsequent ZeroDegree spectrometer (ZDS) [41] before being injected into the ZeroDegree Multi-Reflection Time-of-Flight (ZD MRTOF) system [39], which is illustrated in Figure 1. The RI exiting the ZDS were too energetic (with energies exceeding 100 MeV/u) to be directly stopped within the cryogenic RFGC [33, 44], which was filled with helium gas at a room-temperature-equivalent pressure of 200 mbar at a temperature of approximately 74 K. To match the RI energy to the stopping power of the RFGC [45], a rotatable stainless steel plate with a thickness of 4 mm was positioned in front of the gas cell entrance window. This beam-energy degrader was controlled by a step motor, allowing for precise adjustments in steps of 0.0072°. The angle of the degrader was optimized for each specific RI by measuring the pass-through fraction of each RI [46] as a function of the degrader angle. This was accomplished by measuring the counting rates of plastic scintillators located both upstream and downstream of the RFGC as presented in Section 2.1.

After passing through the energy degrader and entrance window, the incident RI will continue to lose energy through collisions with helium gas. The more energetic of these ions will

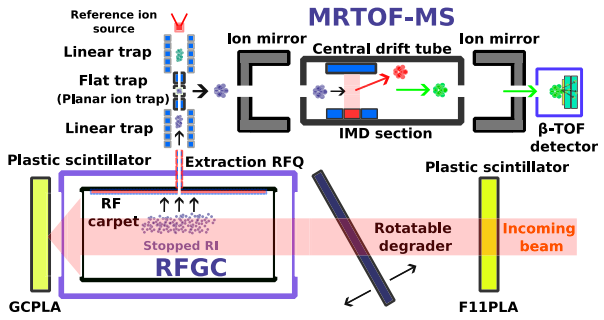

FIGURE 1
Sketch of the experimental setup consisting of a gas cell (RFGC), a triplet ion-trap suite, an MRTOF-MS, and a β-TOF detector. Highly energetic ions from the ZeroDegree spectrometer are entering from the bottom right. Incoming ions and ions transmitted through the gas cell were detected using plastic scintillators. Stopping of ions in the helium was achieved by a rotatable beam-energy degrader. Ions were extracted from the RFGC by a segmented quadrupole RF ion guide and forwarded to an adjacent linear ion trap for ion accumulation. Analyte and reference ions are concomitantly transferred from the linear Paul traps to the flat trap for final cooling prior to injection into the MRTOF-MS. While reflecting, contaminant ions (red ion cloud) are removed by an in-MRTOF deflector, and the purified ensemble (green cloud) eventually hits the β-TOF detector for TOF measurement and detection of subsequent β-decays.

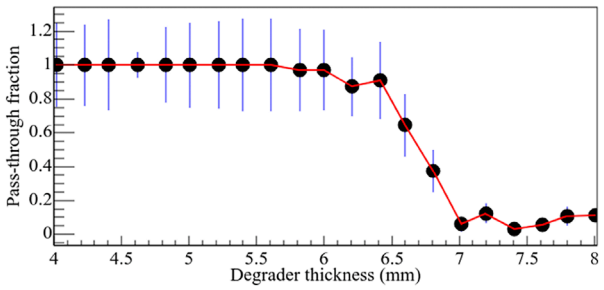

FIGURE 2
Degrader-thickness optimization for ^{75}Ni. The curve shows the ratio of rates detected by GCPLA and F11PLA as a function of the degrader thickness. The profile was used to determine the optimal setting for efficient isotope stopping in the He gas.

reach the end of the gas cell and either stop in the exit window or pass through it and be delivered to downstream apparatuses, while the lower-energy ions will eventually stop and reach thermal equilibrium with the helium gas. A combination of statically biased electrodes and radio-frequency ion carpets provide an electric field that attracts, collects, and transports the RI to the RFGC's exit aperture and then transfers them to a well-established triple ion-trap suite [38, 47, 48] via a small segmented quadrupole RF ion guide. The trap suite consists of a central Paul trap with planar geometry (hereafter: flat trap) with two linear quadrupole ion traps coupling to it from each side – one to accept analyte ions from the RFGC, and the other to accept reference ions from a thermal ion source. The RI and reference ions from the thermal ion source accumulate and further cool down in the linear ion guides, and are concomitantly transferred to the flat trap for final cooling before being ejected into the MRTOF-MS for time-of-flight analysis, with an interval of approximately 25 ms between each reference and analyte sub-cycle (see [42, 49] for details on the timing sequence). The ions undergo back-and-forth reflections by a pair of electrostatic ion mirrors, during which the ions have an average kinetic energy of 2.5 keV/q within the field-free region between the ion mirrors. To mitigate the impact of highly abundant contaminant ions, a parallel-plane in-MRTOF deflector (IMD) is installed within the field-free region to allow generation of a transversal electric field to selectively deflect ions. The generation of the deflection field was synchronized with the lap time of isobaric ion chains of interest, thereby removing contaminant ions from different lap numbers during the multiple-reflection process. After about 700 laps of reflection, corresponding to a time of flight of about 12 ms for the RI, the ions were released and subsequently impacted on the newly developed "β-TOF" ion detector [50] (modified from an ETP 14DM572 MagneTOF [51]) at the end of the flight. The time of the ion-impact signal relative to the signal to eject ions from the flat trap, defining the time-of-flight of an ion, is recorded by an ultra-fast multi-event time-to-digital converter (TDC) (MCS6A, Fast ComTech) with an inherent resolution of 100 ps per time bin [52].

2.1 BigRIPS PID-based optimization of the degrader angle

In order to perform mass measurements in the ZD MR-TOF device, it is necessary to halt the radioactive ion within 500 mm of helium gas. The typical beam energy after the ZeroDegree spectrometer ranges from 100 to 200 MeV/nucleon (3 MeV/nucleon energy distribution when a mono-energetic wedge degrader is used). To effectively decelerate these energetic beams within the helium gas, a thickness-adjustable degrader system was employed. While the optimum degrader thickness for individual ion species of interest can be estimated by LISE++ [53], this value should be fine-tuned experimentally using the F11 plastic detector (F11PLA) and a second plastic detector located downstream of the gas cell (GCPLA). For isotopes with low intensity (rates as low as 1 count/h at the β-TOF detector), directly measuring the rate curve by counting ions with the MRTOF is impractical. In such cases, the ratio of transmitted isotopes can be measured as a function of degrader thickness, which allows for determining the optimum degrader thickness independent of the ion losses during the transport up to the MRTOF-MS. We have developed an online data analysis program for degrader thickness optimization within the frame work of the RIBF data acquisition (DAQ) system [54]. The program provides real-time particle identification (PID) of the RIs before and after entering the gas cell, using the beam-line detectors of BigRIPS in coincidence with F11PLA and GCPLA. Figure 2 demonstrates the optimization of the degrader for ^{75}Ni using a 4 mm thick rotatable stainless steel flat degrader. The ratio between the beam rate detected in the GCPLA and the F11PLA decreases with increasing effective degrader thickness. The optimum degrader thickness depends on the energy distribution of the incoming beam, but typically corresponds to a pass-through fraction of approximately 0.3 ~ 0.5 and can be calibrated using a higher-intensity RI with the MRTOF-MS.

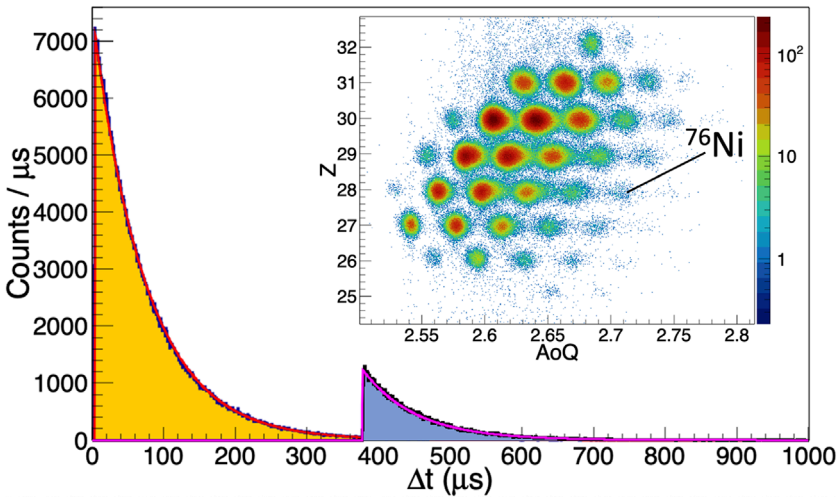

FIGURE 3
Fitted distribution of time intervals between consecutive events measured with the DDAQ system (orange-filled) compared with that obtained using the BigRIPS CAMAC DAQ (blue-filled). The inset presents the associated PID spectrum. The CAMAC DAQ's 337 μs deadtime is clearly visible in the blue-filled curve.

In the present experiment, the RIBF DAQ system utilizing CAMAC-based Analog-to-Digital Converters (ADC) and Time-to-Digital Converters (TDC) were employed for the degrader thickness optimization. However, this system experiences sizable acquisition deadtime, reaching up to 85%, under high-intensity cocktail beams of approximately 13.5 kHz. Such deadtime prolongs the data taking time for degrader optimization of rare events involving exotic nuclei.

To address these limitations, we conducted parallel testing of a Digital DAQ (DDAQ) system based on high-speed digitizers, aimed at acquiring PID data from beamline detectors of the BigRIPS-ZeroDegree spectrometers. Signals from key beamline detectors of ZeroDegree spectrometer, including plastic scintillators at the seventh (F7) and eleventh (F11) BigRIPS focal planes, the Position-Sensitive Parallel Plate Avalanche Counter (PPAC) at the tenth (F10) focal plane, and the Ionization Chamber (IC) at the F11 focal plane, were processed using CAEN V1730 digitizers. These digitizers operated with Digital Pulse Processing for Pulse Shape Discrimination (DPP-PSD) and Pulse Height Analysis (DPP-PHA) firmwares in a channel self-triggered mode [55]. Combining high-resolution timestamp information of down to few tens of picoseconds and energy information for each channel, the DDAQ system enabled online event reconstruction, real-time PID, and reduced data acquisition deadtime.

The performance of the DDAQ system was evaluated by analyzing the deadtime and event rate through a non-paralyzable deadtime model, fitting the distribution of time intervals between consecutive events [56]. Figure 3 illustrates the sizable reduction in deadtime achieved with the DDAQ system compared to the CAMAC-based system. Specifically, the DDAQ system exhibited a deadtime of approximately 4 μs, compared with the 377 μs observed with the CAMAC DAQ. Additionally, a PID plot generated using the DDAQ system, with just a few beamline detectors employed, demonstrates sufficient resolution to identify exotic nuclei.

Following the success of this test, the DDAQ system was further employed to read out Time-of-Flight (TOF) signals from the ZD MRTOF system. The TOF events recorded by the MRTOF stop detector were time-stamped, enabling the correlation of events between two independent PID methods: those derived from the ZeroDegree beamline detectors and the MRTOF Mass Spectrometer (MRTOF-MS). This capability facilitated online monitoring of the absolute efficiency of the RFGC and ZD MRTOF setup.

2.2 On-line application of the multi-mass protection mode with an IMD

An unavoidable characteristic of the MRTOF-MS is that ions with different A/q values appear in the time-of-flight spectrum with different numbers of revolutions. When there are few impurity ions, it is possible to distinguish whether a given signal corresponds to the analyte A/q ion or not by changing the number of measurement revolutions by at least one [57]. However, impurities dominate in many online measurements, making their removal a critical challenge.

To this end, purification using an IMD has been implemented at several facilities [58–60]. The simplest method of selection is to roughly restrict the mass range by adjusting the timing of the pulses applied to the IMD at the ion injection stage. Furthermore, periodically applying pulses was demonstrated for the transmission of a single chosen A/q. In the present study, a selection more ideal to in-flight cocktail beams was achieved by applying a highly refined pulse sequence to allow multiple arbitrary mass ranges to pass safely.

To perform effective mass selection with the IMD while maintaining high-precision mass measurement accuracy, it is necessary to set appropriate pulse amplitude, timing, and pulse count. Particular care must be taken when measuring ions with multiple A/q values. During the several hundred round trips, there are certain moments when multiple analyte ions pass through the

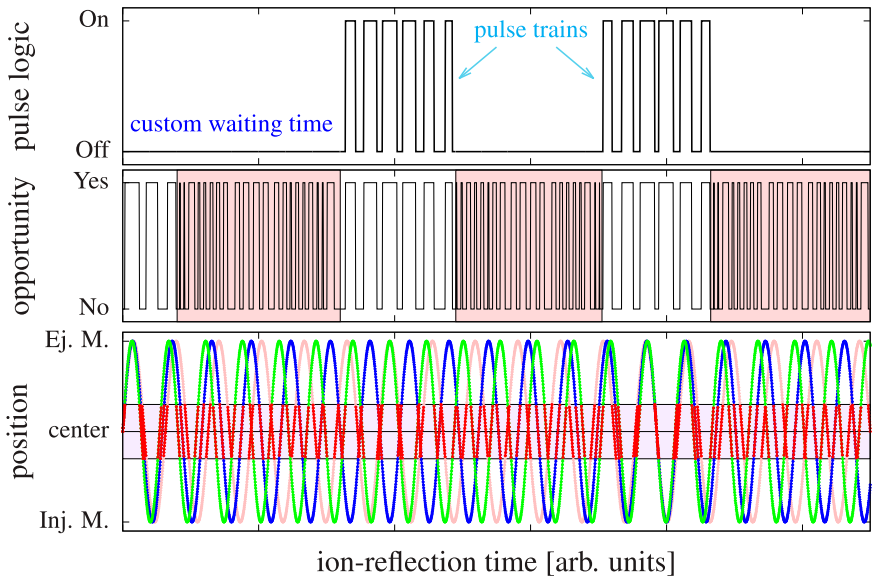

FIGURE 4
Example for a pulse pattern to protect ions of three different masses, with a mass difference of 8% to each other. The top part shows the logic of the pulse signal, the middle part shows opportunities to switch the deflector when none of the ions is in the affected region, and the bottom part illustrates the simplified ion positions (each mass with different color) during reflection between injection mirror and ejection mirror. The shaded region in the bottom, in which red color is used for the ion position, denotes the zone in which an ion would be influenced if the deflector voltage is present during crossing. The red shaded region in the top illustrates a time interval in which only short deflector pulses could be applied as the ions are not passing the IMD at similar times. In such time intervals IMD pulses are omitted.

deflection electrodes nearly simultaneously. By using only those limited time windows, pulses are applied to the deflection electrodes only when all of the analyte ions are sufficiently far from the deflection electrodes during both the forward and return paths. To provide a visualization of this timing scheme, a simplified example for ion motion and pulse pattern is shown in Figure 4. If the desired analyte ions are too dispersed in timing, however, there can be effectively no opportunity to apply removal pulses. In that way, pulses are applied when the on-time can be sufficiently long. Similarly, the choice of the desired analyte masses must occasionally be reduced to limit the off-time of the deflector and ensure efficient broadband ejection of unwanted ions.

Since the trajectories of all A/q ions can be accurately determined from the revolution number and flight time of a reference ion, the valid pulse application timings can be calculated numerically. In a typical case (e.g. three different mass units with A ≈ 100), four convenient time windows can be found within 4 ms and 8 ms flight time, during which approximately 30 deflection pulses (20–30 V) are applied (120 pulses in total). This allows the removal of unwanted A/q ions without affecting the time-of-flight (ToF) of the required ions. By applying properly configured pulses in the later stages of the revolutions, this method is also used to remove heavy isobaric molecular ions, or to eliminate longer-lived nuclei (near the line of stability) to reduce background in the β-ToF detector.

In Figure 5, two IMD-purified spectra from reaction products delivered by BigRIPS are shown: visibly clean due to the selected transmission. At the ZD MRTOF system, it is typically possible to select up to four simultaneously selected isobaric chains without degrading operation, depending on the particular selection. Choosing the transmitted isobaric chains must be carefully done to avoid an overlapping of ion peaks. Depending on the prior knowledge of the expected spectrum, more or wider mass ranges can be selected subsequently to provide clarification. In Figure 5 we provide examples of well-chosen (bottom) and poorly chosen (top) timing parameters. In the latter unwanted ion transport resulting in overlapping isobar chains can be seen, where $A/q = 78/2$ ions have been erroneously transmitted along with $A/q = 75/2, 76/2, 77/2$ ions and appear at similar times-of-flight.

2.3 First on-line application of a β-TOF detector

The newly developed β-TOF detector [50] comprises a stack of two 500 μm-thick silicon solid-state detectors (SSDs, Hamamatsu S-14605) installed within the impact plate of a 14DM572 MagneTOF, enabling the detection of ion impact and subsequent β-decay using a single detector unit. The surface of the top SSD was coated with a 10 nm gold layer and a 5 nm Al_2O_3 layer to enhance the emission of secondary electrons following the impact of incident ions. As illustrated in Figure 6A), these emitted secondary electrons are guided to an electron multiplier by the superposed electric and magnetic fields of the ETP MagneToF detector, generating a distinct electronic pulse as the signal of ion impact for the time-of-flight measurement. Furthermore, when β-unstable RIs have been stopped in the β-TOF detector, subsequently emitted β-particles could pass through and trigger the two SSDs, forming a $\Delta E - \Delta E$ telescope for β event identification. The energy signals from the two SSDs were amplified by shaping amplifiers and

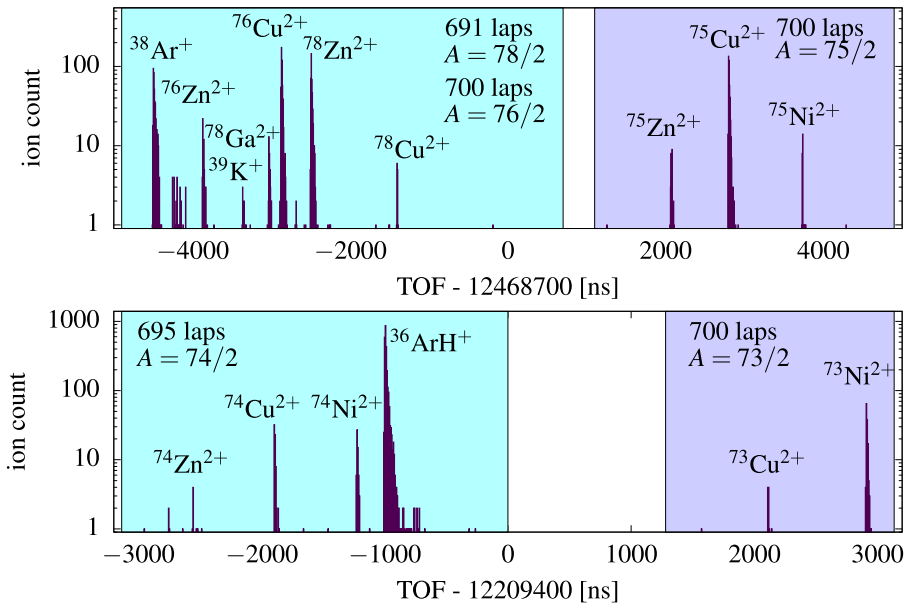

FIGURE 5
Top: Time-of-flight spectrum for A/q = 75/2, 76/2, 78/2 isobars (radioactive ions in 2^+ state), where the IMD has been preset to transmit A/q = 75/2, 76/2, 77/2 (A/q = 77/2 not abundant). Color shades indicate expected regions for different isobar chains. One can see limitations due to the presence of $^{78}Ga/Zn/Cu^{2+}$ ions transmitted along with the other isobar chains without intention (see text). Bottom: Time-of-flight spectrum of A/q = 73/2 and A/q = 74/2 isobars.

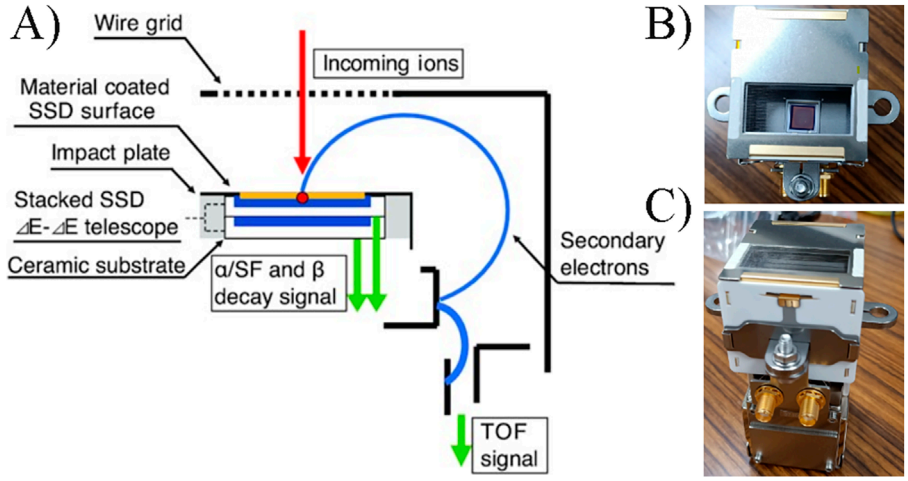

FIGURE 6
(A) Schematic of the β–TOF detector taken from Ref. [50]. **(B,C)** are photos of the β–TOF detector. **(B)** shows the entrance of the detector. Through the wire grid, the front-side SSD – implanted into the impact plate of the detector – is visible. **(C)** shows two additional SMA connectors, which were added for the signal outputs from the two SSDs inside the detector.

recorded using a portable USB analog-to-digital converter (USB-ADC, TechnoAP APG7400A [61]). The USB-ADC also recorded the synchronized signal of ion ejection from the ion trap for β-decay and TOF correlation measurements.

Figure 7 illustrates the procedure for evaluating β-TOF correlated measurements. Signals from both SSDs are continuously recorded with timestamps provided by the internal clock of the USB-ADC. To identify candidates for β-decay events, a 1 μs coincidence window $\Delta T_{\beta-\beta}$ is opened for each event detected on one SSD. If a signal from the other SSD occurs within this window, the pair is considered a β-event candidate. Flat-trap ejection triggers are additionally recorded by the USB-ADC, allowing the determination of the time-of-flight signal timestamps from the MRTOF-MS within the same time reference. For each TOF event, a decay-time window $\Delta T_{\beta-TOF} \equiv [-10 \times T_{1/2}, +10 \times T_{1/2}]$ is applied, where $T_{1/2}$ is the expected half-life of the ion of interest. Any β-event candidate

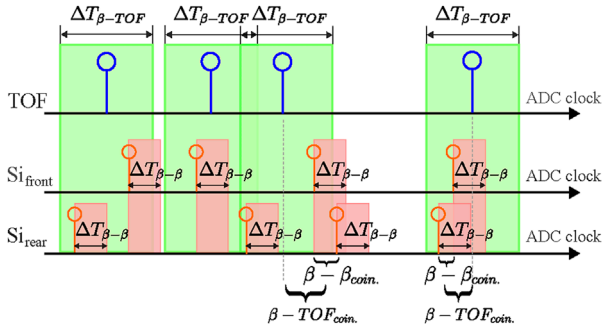

FIGURE 7
Schematic illustration of β-β and β-TOF coincidence events. Events detected by the TOF and silicon detectors are represented by blue and red circles, respectively. The green and red filled rectangles indicate the time windows defined by the corresponding TOF and β events for the β-TOF and $\beta-\beta$ correlated measurements, respectively. Note that the time windows are not drawn to scale for clarity.

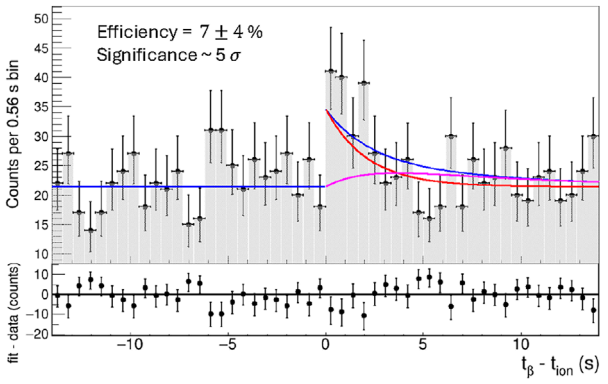

FIGURE 8
Measurement example for β-TOF coincident events using ^{78}Zn ($T_{1/2}$ = 1.47(15) s from [62]), which was available in higher quantities during the experiment. The top panel displays the decay curve fitted with the Bateman equation (blue), incorporating parent (red) and descendant nuclei (purple) in the decay chain with half-lives fixed to literature values. The bottom panel shows the residuals between the data and the fit. The background fit was performed using uncorrelated events before ion impact, while the fit range for the decay starts with the ion impact time and continues for several half lives of the expected isotope.

falling within this window is registered as coincident with the corresponding TOF event. The time difference between the β event and the TOF event is defined as a possible decay time of the ion, where β events occurring prior to the TOF signal (i.e., negative decay time) are used to estimate the β-background distribution. As background may arise from uncorrelated β decays of other radioactive ions or from accidental coincidences of electronic noise between the SSDs, these random events contribute a uniform background in the decay-time distribution. In contrast, the true β decays correlated with the ions of interest accumulate to form an exponential decay profile in the histogram, becoming prominent with increased statistics.

An example of successful β-TOF correlation is shown for the case of ^{78}Zn in Figure 8. In the example shown, decay correlation is demonstrated through an unbinned fit of the decay curve data, describing the activity evolution of parent and descendant nuclei. A statistical significance of approximately 5σ were determined using the Profile Likelihood method within the RooStats framework.

In this first effort using the β-TOF detector on-line, however, intense background events were observed. The background originated from electronic noise and β-decay of RI deposited on the SSD. Since the SSDs were implanted inside the MagneTOF detector, they inevitably picked up noise from Zener diodes within the commercial detector, which contributes to the major part of the low-energy counts from the two SSDs, especially the one at the entrance side. To suppress accidental $\beta-\beta$ coincidences from noise in both SSDs and to prevent overloading the SSD data acquisition system at high throughput rate, high detection thresholds – equivalent to approximately 160 keV – were applied to both channels of the USB-ADC. In addition, the design used in this study has an insulating ceramic layer (0.8 mm) between the two SSDs, where a simulation reveals that the coincidence efficiency is about 11% (*i.e.*, a fraction of low-energy β particles cannot penetrate to the second SSD). These factors limit the detector efficiency, where measurement and simulation (~10% detection efficiency) have been in agreement when testing with ^{78}Zn. Despite the high baseline noise, β-β coincidence measurements effectively suppress accidental coincidences caused by electronic noise. For instance, in the case of ^{78}Zn, the β counting rate decreased dramatically from approximately 0.05 cps during beam-on periods to 0.0007 cps in post-beam measurements. This sharp reduction indicates that the dominant source of the observed β background was the true β-decay of RI deposited on the front-facing SSD.

In upcoming efforts, effective background suppression will be a key focus. Both implanted RIs and electronic noise must be mitigated to improve the signal-to-noise ratio of β-TOF measurements. Strategies include careful use of the IMD and implementation of tighter slit settings in BigRIPS to reduce the total number of RI deposited on the SSD. Additionally, integrating a fast-switching power supply to promptly disable the MagneTOF upon detection of an ion of interest would allow subsequent β decays to be captured in a quieter electronic environment [63]. Moreover, half-life measurements under non-zero background conditions remain an important topic for further investigation with this new detector setup. In clean conditions (β-TOF detector not contaminated), a detection yield of several tens of ions per hour would be sufficient for the purpose of half-life measurements. This application is particularly interesting for assignments of ground state and isomer separated by mass, if the corresponding half-lives differ sufficiently. The present study validates the major purpose of the application, which is to distinguish the RI from stable intruder molecular ions in the TOF spectra.

3 Data analysis

Due to the instability of voltages applied to electrodes of the MRTOF-MS as well as thermal expansion from temperature fluctuations, the TOF of ions drifts during the measuring time. A software drift correction was performed to recover the high resolution of the TOF spectrum. After drift correction, fitting

procedures were applied to extract the peak center of the ion of interest. The high-order ion optical aberration of the mirrors and low-angle scattering of ions by residual gas in the MRTOF-MS resulted in an asymmetric spectral peak shape. To approximate the peak shape, the Gaussian-exponential hybrid function of Equation 1 was applied in the fitting process to extract the central TOF of a peak by the maximum log-likelihood method. In the fitting function, t_m denotes the peak center of the central Gaussian component and represents the ion's TOF. The shape of the distribution is characterized by five parameters: σ, t_L, t_R, t_{r1}, and k_1. Here, σ is the standard deviation of the central Gaussian. The parameters t_L ($t_L < 0$) and t_R ($t_R > 0$) define the transition points from the Gaussian peak to the left and right exponential tails, respectively, relative to t_m. The parameter t_{r1} specifies the onset of a secondary exponential tail on the right side, measured from t_m, and k_1 ($k_1 > 0$) is its corresponding decay constant. These shape parameters are determined by fitting the most intense ion peak, which usually serves as the reference ion, to inhibit the influence of peak shape. These parameters were then fixed, leaving only amplitude and peak position as free parameters during the fitting process to extract the TOF of other peaks in the same spectrum. In the following example, Figure 9a, $^{39}K^+$ from a thermal ion source was selected as reference ions. Fitting for $^{39}K^+$ was first performed to determine shape parameters, which were then fixed in the fitting routine in order to extract the TOF of $^{75}Ni^{2+}$, Figure 9b. The spectrum was measured with $^{75}Ni^{2+}$ making 700 laps, corresponding to a flight path of ~1 km. The mass resolving power, $R_m = t/2t_{FWHM}$, of $^{75}Ni^{2+}$ in this spectrum was evaluated to be $\sim 6 \times 10^5$, indicating the high mass resolving power that was achieved in this work.

$$f(t) = \begin{cases} A \cdot \exp\left(\dfrac{t_L\left(t_L - 2\left(t - t_m\right)\right)}{2\sigma^2}\right), & t < t_m + t_L \\ A \cdot \exp\left(-\dfrac{\left(t - t_m\right)^2}{2\sigma^2}\right), & t \in \left[t_m + t_L, t_m + t_R\right) \\ A \cdot \exp\left(\dfrac{t_R\left(t_R - 2\left(t - t_m\right)\right)}{2\sigma^2}\right), & t \in \left[t_m + t_R, t_m + t_{r1}\right) \\ A \cdot \exp\left[\begin{array}{c} \dfrac{t_R}{\sigma^2}\left(\dfrac{t_R}{2} - t_{r1}\right) \\ -k_1\left(t - \left(t_m + t_{r1}\right)\right) \end{array}\right], & t \geq t_m + t_{r1} \end{cases} \tag{1}$$

The relation between TOF (t) and the mass-to-charge ratio (m/q) of an ion is expressed as

$$t = a\sqrt{m/q} + t_0, \tag{2}$$

where a is a constant related to the device characteristics and t_0 is a time offset for the delay from the start trigger of TDC to the actual ejection of an ion. By measuring the TOF of the reference ion with a well-known mass and following Equation 2, the mass of the analyte can be given by Equation 3

$$m_x = m_{ref}\frac{q_x}{q_{ref}}\left(\frac{t_x - t_0}{t_{ref} - t_0}\right)^2 = m_{ref}\frac{q_x}{q_{ref}}\rho^2, \tag{3}$$

where t_x, m_x, and q_x denote the TOF, mass, and charge of the analyte ion of interest, respectively, while t_{ref}, m_{ref}, and q_{ref} represent the corresponding quantities for the reference ion. The ratio $\rho = (t_x - t_0)/(t_{ref} - t_0)$ in Equation 3 therefore characterizes the ratio of the actual TOF of the analyte to that of the reference ion. In addition to radioactive ions, stable molecular ions with precisely known atomic mass values, such as $^{36}Ar^1H^+$ were also observed in the spectra, providing useful benchmarks for t_0 calibration. By adjusting t_0 to align the measurement of $^{36}Ar^1H$ to agree with literature values given in AME2020 [64] and considering the 1σ error band, t_0 was evaluated to be 82.5 (2.5) ns. As noted in Ref. [65] and Ref. [66], using an isobaric reference ion results in a relative systematic mass uncertainty $\delta m/m$ from δt_0 of about 10^{-9}, corresponding to ~0.1 keV in the mass range of this work—negligible compared to statistical uncertainties. When an isobaric reference is unavailable, a non-isobaric ion is used. In such cases herein, the relative mass deviation from the AME value, defined as $\Delta m_{exp}/m_{AME} = (m_{exp} - m_{AME})/m_{AME}$, has been estimated to be approximately $-5 \times 10^{-8}/(A/q)$, based on recent offline evaluations of the systematic uncertainty.

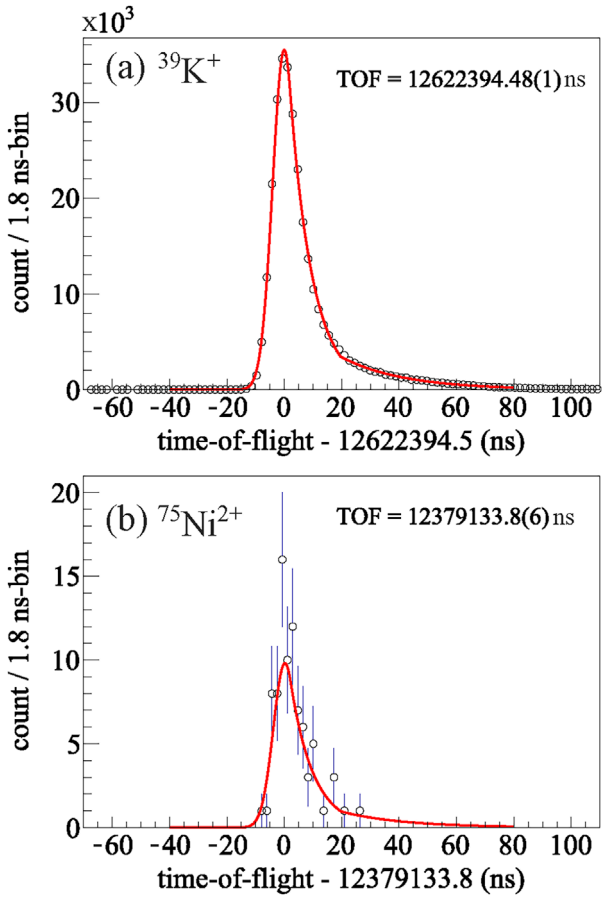

FIGURE 9
Time-of-flight spectra for **(a)** $^{39}K^+$ and **(b)** $^{75}Ni^{2+}$ after 700 laps in the MRTOF-MS. Shape parameters used for the fitting of analyte spectral peaks were determined from the profile of the $^{39}K^+$ spectral peak.

4 Mass measurement results

The mass results of the analyzed data set are shown in Table 1; Figure 10. In the recent literature, two high-precision

TABLE 1 Measured isotopes, the reference ion, effective time-of-flight ratios ρ, measured mass excess ME_{MRTOF}, mass excess from literature AME2020 [64], and mass deviation calculated as $\Delta m = ME_{MRTOF} - ME_{AME20}$.

Species	Ref. ion	ρ	ME_{MRTOF} (keV/c^2)	$ME_{AME2020}$ (keV/c^2)	Δm (keV/c^2)
$^{73}Ni^{2+}$	$^{73}Cu^{+}$	1.000065381 (162)	−50103 (22)	−50108.2 (24)	5 (22)
$^{37}Cl^{+}$	$^{39}K^{+}$	0.9740256420 (874)	−31756.8 (62)	−31761.552 (52)	4.7 (62)
$^{36}Ar^{1}H^{+}$	$^{39}K^{+}$	0.9741502982 (53)	−22942.78 (37)	−22942.571 (26)	−0.21 (37)
$^{74}Ni^{2+}$	$^{39}K^{+}$	0.9741322240 (331)	−48441.7 (47)	$-48700^{\#}(200^{\#})$	$258^{\#}(200^{\#})$
$^{74}Cu^{2+}$	$^{39}K^{+}$	0.9740786414 (703)	−56019.1 (99)	−56006.2 (61)	−13 (12)
$^{74}Zn^{2+}$	$^{39}K^{+}$	0.974009888 (100)	−65741 (14)	−65756.7 (25)	15 (14)
$^{75}Ni^{2+}$	$^{39}K^{+}$	0.9807276839 (443)	−44045.4 (63)	$-44240^{\#}(200^{\#})$	$195^{\#}(200^{\#})$
$^{75}Cu^{2+}$	$^{39}K^{+}$	0.9806544630 (236)	−54470.0 (34)	−54470.22 (72)	0.2 (34)
$^{75}Zn^{2+}$	$^{39}K^{+}$	0.9805975627 (888)	−62571 (13)	−62558.9 (20)	−12 (13)
$^{76}Cu^{2+}$	$^{39}K^{+}$	0.9872000112 (200)	−50982.1 (29)	−50981.63 (91)	−0.5 (30)
$^{76}Zn^{2+}$	$^{39}K^{+}$	0.9871210570 (628)	−62297.2 (90)	−62303.0 (15)	5.8 (91)
$^{38}Ar^{+}$	$^{39}K^{+}$	0.9870713219 (190)	−34712.2 (14)	−34714.83 (20)	2.7 (14)
$^{77}Cu^{2+}$	$^{77}Zn^{2+}$	1.000069303 (161)	−48856 (23)	−48862.8 (12)	7 (23)
$^{77m}Zn^{2+}$	$^{77}Zn^{2+}$	1.000005259 (241)	−58035 (35)	−58016.8 (20)	−19 (35)
$^{78}Cu^{2+}$	$^{38}Ar^{1}H^{+}$	1.000069249 (146)	−44787 (23)	−44789 (13)	2 (26)
	$^{78}Zn^{2+}$	1.0000874270 (982)	−44789 (14)	−44789 (13)	1 (20)
			−44788 (12)*	−44789 (13)	1 (18)*
$^{78}Zn^{2+}$	$^{38}Ar^{1}H^{+}$	0.9999820088 (366)	−57464.0 (53)	−57483.2 (19)	19.2 (57)
$^{78}Ga^{2+}$	$^{38}Ar^{1}H^{+}$	0.999939351 (169)	−63660 (28)	−63704.1 (11)	44 (28)
	$^{78}Zn^{2+}$	0.999957271 (368)	−63694 (40)	−63704.1 (11)	10 (40)
			−63671 (23)*	−63704.1 (11)	33 (23)*
$^{38}Ar^{1}H^{+}$	$^{78}Zn^{2+}$	1.0000181264 (468)	−27425.7 (35)	−27425.86 (19)	0.2 (35)

Extrapolated values of AME2020 are denoted by #. For isotopes measured with more than one reference ion, the mean of their measurements is denoted by an ∗.

mass measurement campaigns focused on the shell evolution of neutron-rich Ni isotopes have been reported. In 2017, the masses of copper isotopes were measured at ISOLDE up to ^{79}Cu, where large-scale shell-model calculations including a model space up to 8*p*8*h* (8 protons, 8 holes) configurations were performed, and support a doubly-magic character of ^{78}Ni [11] using the data of Cu masses. More recently, in 2022, the masses of Ni isotopes were successfully measured at JYFLTRAP, reaching the isotope ^{75}Ni for the first time, and have been reported in an astrophysical context [19]. In our complementary study, atomic masses for a total of sixteen radioactive isotope have been precisely measured, allowing comparison with the two preceding publications and the AME2020 data. For the isotopes ^{74,75}Ni, deviations of $m_{exp} - m_{AME} = 249(200)$ keV and 184(201) keV, respectively, compared to the AME2020 extrapolation were previously observed [19]. Our measurements of ^{74,75}Ni masses in this work agree within about 10 keV with these recent results from JYFLTRAP. A similar agreement is obtained for the masses of ^{77,78}Cu, in comparison with the previously reported values from ISOLTRAP [11]. Furthermore, we find agreement to the AME2020 mass data for radioactive and stable ion species.

Giraud et al. [19] have studied the impact of newly measured masses of ^{74,75}Ni on the electron-capture rates and eventually the core-collapse supernova dynamics. In this work, we further explore

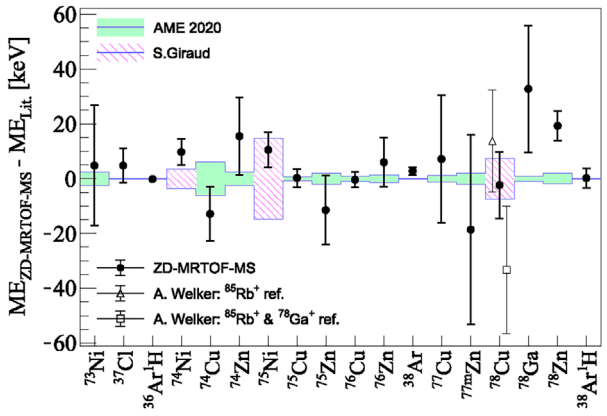

FIGURE 10
Deviations of the measured isotope masses from the AME2020 values are shown, except for ^{74,75}Ni and ^{78}Cu, whose deviations are taken relative to the values in Ref. [19]. Measurements of ^{78}Cu using a single reference ion (^{85}Rb^{+}) and using two reference ions (^{85}Rb^{+} and ^{78}Ga^{+}) from Ref. [11] are denoted by the hollow triangle and square, respectively.

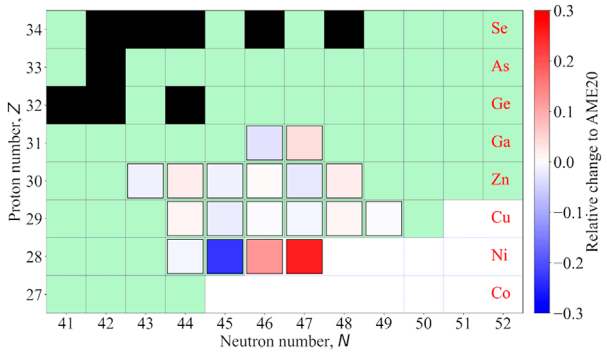

FIGURE 11
Isotope chart with color-coded changes of σv at T = 1 GK obtained from calculations with different input mass values. The color scale represents the relative difference between reaction rates calculated using TALYS 1.96 with the new mass values from this work (σv_{exp}) and those using masses from AME2020 ($\sigma v_{AME2020}$). The relative change is defined as $(\sigma v_{exp} - \sigma v_{AME2020})/\sigma v_{AME2020}$. Nuclei with known masses (AME2020) and stable are showed as light and black box, respectively.

the impact of our newly measured mass values on the neutron capture rate in the *r*-process. We follow the framework of [66] and use the mass results to investigate the impact on neutron-capture reaction rates (σ_v) for the isotopes in question. To this end, the nuclear reaction modeling code TALYS 1.96 was used with default settings for the optical model potentials, level densities, and γ-ray strength functions. Figure 11 show the relative change in reaction rates at the standard *r*-process temperature of $T = 1$ GK, calculated using using the mass values from this work and those listed in the AME2020 [64]. The most pronounced changes in (n, γ) reaction rates are obtained for $^{73\text{-}75}$Ni with an increase of about 30 % for ^{75}Ni. The sensitivities of r-process trajectories to neutron-capture rates have been studied in Ref. [67], where neutron-rich isotopes with $Z = 26 - 34$ have been set into relation in Figure 7 of Ref. [67]. Changes of σ_v for the isotopes $^{73\text{-}75}$Ni moderately affect the production of elements in the weak *r*-process, whereas the highest impact for the Ni chain is expected for ^{76}Ni, for which high-precision mass measurements have yet to be performed.

5 Conclusion

In summary, three novel methods (and devices) were tested on-line for the first time in two multi-reflection time-of-flight mass measurement campaigns focused on neutron-rich Ni isotopes:

- Particle-identification based transmission measurements were employed to accelerate the optimization of the flat-degrader thickness into order to maximally stop ions in the gas cell. A newly implemented DDAQ system provided real-time particle identification (PID) with a dead time reduced by approximately two orders of magnitude, offering significantly improved data acquisition efficiency compared to the existing RIBF DAQ system based on CAMAC.
- An advanced pulse pattern applied to an in-MRTOF deflector (IMD) allowed for selective retention of ions with individually selected mass-to-charge ratios, while preventing the transport of unselected ions. Clean TOF spectra with more than one mass unit at the same time have been obtained for radioactive ions, allowing for simultaneous measurements.
- The introduction of the novel β-TOF detector enabled identification of ions, and to distinguish radioactive species from stable molecules. This method also allowed for an approximate half-life evaluation of the radioactive ions. In this first application, the analysis could be demonstrated with abundant ion species such as ^{78}Zn through correlated measurements of β-decay and time-of-flight. However, high radiation background prevented the application for challenging (*i.e.*, low-yield) cases.

In total, seventeen isotopes have been analyzed within these experiments, wherein ^{78}Cu and ^{73,74,75}Ni are the most exotic cases. The atomic mass values have been compared to other recently published values, where agreement was found within the 1-σ measurement uncertainties. The atomic mass results have further been used to calculate r-process neutron-capture cross sections for the nuclei of interest. For future β-decay correlated measurements the present work denotes a proof of principle, while further work is required for selection of ADC threshold settings, shaping amplifier parameters, and understanding the effects of beam intensity in order to enhance the signal-to-noise ratio and optimize the performance of the detection system. New designs for higher β-detection efficiencies are under discussion.

Data availability statement

The raw data supporting the conclusions of this article will be made available by the authors upon reasonable request.

Author contributions

WX: Writing – original draft, Writing – review and editing. MR: Writing – review and editing, Writing – original draft. VP: Writing – review and editing, Writing – original draft. MW: Writing – review and editing. PS: Writing – review and editing. DH: Writing – review and editing. AT: Writing – review and editing. SC: Writing – review and editing. TN: Writing – review and editing. YH: Writing – review and editing. HI: Writing – review and editing. SI: Writing – review and editing. YI: Writing – review and editing. TK: Writing – review and editing. SK: Writing – review and editing. JLi: Writing – review and editing. JLe: Writing – review and editing. SM: Writing – review and editing. HM: Writing – review and editing. JM: Writing – review and editing. MM: Writing – review and editing. SNi: Writing – review and editing. SNa: Writing – review and editing. TS: Writing – review and editing. YW: Writing – review and editing. HW: Writing – review and editing. SY: Writing – review and editing.

Funding

The author(s) declare that financial support was received for the research and/or publication of this article. This work was supported by the National Research Foundation (NRF) grant (TOPTIER, RS-2024-00436392) by the Korea government of Ministry of Science and ICT (MSIT), the Japan Society for the Promotion of Science KAKENHI (Grants: 24224008, 17H06090, 18K13573, 18H05462, 19K14750, 20H05648, 21J00670, 21K13951, 22H01257, 22H04946, and 25H01273), the RIKEN Junior Research Associate Program, the RIKEN program for Evolution of Matter in the Universe (r-EMU) and RiNA-Net, Research Grants Council (RGC) of Hong Kong with a grant of General Research Funding (GRF-17312522). We acknowledge support from KAKENHI No. 23K13132 for the development of β-TOF detector.

Acknowledgements

We express our gratitude to the RIKEN Nishina Center for Accelerator-based Science.

Conflict of interest

The authors declare that the research was conducted in the absence of any commercial or financial relationships that could be construed as a potential conflict of interest.

The reviewer AIML declared a past co-authorship with the author(s) VP, SN to the handling editor.

Generative AI statement

The author(s) declare that no Generative AI was used in the creation of this manuscript.

Any alternative text (alt text) provided alongside figures in this article has been generated by Frontiers with the support of artificial intelligence and reasonable efforts have been made to ensure accuracy, including review by the authors wherever possible. If you identify any issues, please contact us.

Publisher's note

References

1. Engelmann C, Ameil F, Armbruster P, Bernas M, Czajkowski S, Dessagne P, et al. Production and identification of heavy ni isotopes: evidence for the doubly magic nucleus $^{78}_{28}$Ni. *Z für Physik A Hadrons Nuclei* (1995) 352:351–2. doi:10.1007/bf01299748

2. Otsuka T. Exotic nuclei and nuclear forces. *Physica Scripta* (2013) 2013:014007. doi:10.1088/0031-8949/2013/t152/014007

3. Hagen G, Jansen G, Papenbrock T. Structure of ^{78}Ni from first-principles computations. *Phys Rev Lett* (2016) 117:172501. doi:10.1103/physrevlett.117.172501

4. Nowacki F, Poves A, Caurier E, Bounthong B. Shape coexistence in ^{78}Ni as the portal to the fifth island of inversion. *Phys Rev Lett* (2016) 117:272501. doi:10.1103/physrevlett.117.272501

5. Nowacki F, Obertelli A, Poves A. The neutron-rich edge of the nuclear landscape: experiment and theory. *Prog Part Nucl Phys* (2021) 120:103866. doi:10.1016/j.ppnp.2021.103866

6. Xu ZC, Hu RZ, Jin SL, Hou JH, Zhang S, Xu FR. Collectivity of nuclei near the exotic doubly magic ^{78}Ni by *ab initio* calculations. *Phys Rev C* (2024) 110:024308. doi:10.1103/physrevc.110.024308

7. Sorlin O, Porquet M-G. Nuclear magic numbers: new features far from stability. *Prog Part Nucl Phys* (2008) 61:602–73. doi:10.1016/j.ppnp.2008.05.001

8. Sieja K, Nowacki F. Shell quenching in ^{78}Ni: a hint from the structure of neutron-rich copper isotopes. *Phys Rev C* (2010) 81:061303. doi:10.1103/physrevc.81.061303

9. Xu ZY, Nishimura S, Lorusso G, Browne F, Doornenbal P, Gey G, et al. β-decay half-lives of ^{76,77}Co, ^{79,80}Ni, and ^{81}Cu: experimental indication of a doubly magic ^{78}Ni. *Phys Rev Lett* (2014) 113:032505. doi:10.1103/PhysRevLett.113.032505

10. Orlandi R, Mücher D, Raabe R, Jungclaus A, Pain S, Bildstein V, et al. Single-neutron orbits near 78ni: spectroscopy of the n=49 isotope 79zn. *Phys Lett B* (2015) 740:298–302. doi:10.1016/j.physletb.2014.12.006

11. Welker A, Althubiti N, Atanasov D, Blaum K, Cocolios T, Herfurth F, et al. Binding energy of ^{79}Cu: probing the structure of the doubly magic ^{78}Ni from only one proton away. *Phys Rev Lett* (2017) 119:192502. doi:10.1103/physrevlett.119.192502

12. Taniuchi R, Santamaria C, Doornenbal P, Obertelli A, Yoneda K, Authelet G, et al. 78ni revealed as a doubly magic stronghold against nuclear deformation. *Nature* (2019) 569:53–8. doi:10.1038/s41586-019-1155-x

13. Van de Walle J, et al. Coulomb excitation of neutron-rich Zn isotopes: first observation of the 2(1)+ state in 80Zn. *Phys Rev Lett* (2007) 99:142501. doi:10.1103/PhysRevLett.99.142501

14. Yang XF, Wraith C, Xie L, Babcock C, Billowes J, Bissell M, et al. Isomer shift and magnetic moment of the long-lived $1/2^+$ isomer in $_{30}{}^{79}$zn$_{49}$: signature of shape coexistence near ^{78}Ni. *Phys Rev Lett* (2016) 116:182502. doi:10.1103/physrevlett.116.182502

15. Gottardo A, Verney D, Delafosse C, Ibrahim F, Roussière B, Sotty C, et al. First evidence of shape coexistence in the 78Ni region: intruder 0+2 state in 80 Ge. *Phys Rev Lett* (2016) 116:182501. doi:10.1103/physrevlett.116.182501

16. Schatz H, et al. The half-life of the doubly-magic r-process nucleus 78ni. In: *The 4th international conference on exotic nuclei and atomic masses*. Berlin, Heidelberg: Springer Berlin Heidelberg (2005). p. 639–42.

17. Madurga M, Paulauskas S, Grzywacz R, Miller D, Bardayan D, Batchelder J, et al. Evidence for gamow-teller decay of ^{78}Ni core from beta-delayed neutron emission studies. *Phys Rev Lett* (2016) 117:092502. doi:10.1103/physrevlett.117.092502

18. Ogata K, Bertulani CA. Nuclear medium effect on neutron capture reactions during neutron star mergers. *J Phys G: Nucl Part Phys* (2020) 47:095101. doi:10.1088/1361-6471/ab9d06

19. Giraud S, Canete L, Bastin B, Kankainen A, Fantina A, Gulminelli F, et al. Mass measurements towards doubly magic 78ni: hydrodynamics versus nuclear mass contribution in core-collapse supernovae. *Phys Lett B* (2022) 833:137309. doi:10.1016/j.physletb.2022.137309

20. Tolosa-Delgado A, et al. Impact of newly measured β-delayed neutron emitters around 78Ni on light element nucleosynthesis in the neutrino-wind following a neutron star merger (2025).

21. Wolf RN, Beck D, Blaum K, Böhm C, Borgmann C, Breitenfeldt M, et al. Plumbing neutron stars to new depths with the binding energy of the exotic nuclide ^{82}Zn. *Phys Rev Lett* (2013) 110:041101. doi:10.1103/physrevlett.110.041101

22. Kugler E. The isolde facility. *Hyperfine Interactions* (2000) 129:23–42. doi:10.1023/a:1012603025802

23. Rosenbusch M, Atanasov D, Blaum K, Borgmann C, Kreim S, Lunney D, et al. Ion bunch stacking in a penning trap after purification in an electrostatic mirror trap. *Appl Phys B* (2014) 114:147–55. doi:10.1007/s00340-013-5702-0

24. Beck S, Kootte B, Dedes I, Dickel T, Kwiatkowski A, Lykiardopoulou EM, et al. Mass measurements of neutron-deficient yb isotopes and nuclear structure at the extreme proton-rich side of the n = 82 shell. *Phys Rev Lett* (2021) 127:112501. doi:10.1103/physrevlett.127.112501

25. Mukherjee M, Beck D, Blaum K, Bollen G, Dilling J, George S, et al. Isoltrap: an on-line penning trap for mass spectrometry on short-lived nuclides. *Eur Phys J* (2008) 35:1–29. doi:10.1140/epja/i2007-10528-9

26. Eronen T, et al. Jyfltrap: a penning trap for precision mass spectroscopy and isobaric purification. In: J Äystö, T Eronen, A Jokinen, A Kankainen, ID Moore, H Penttilä, editors. *Three decades of research using igisol technique at the university of Jyväskylä: a portrait of the ion guide isotope separator on-line facility in Jyväskylä*. Dordrecht: Springer Netherlands (2014). p. 61–81.

27. Kwiatkowski AA, et al. Titan: an ion trap facility for on-line mass measurement experiments. In: J Dilling, R Krücken, L Merminga, editors. *ISAC and ARIEL: the TRIUMF radioactive beam facilities and the scientific program*. Dordrecht: Springer Netherlands (2014). p. 143–55.

28. Wolf R, Wienholtz F, Atanasov D, Beck D, Blaum K, Borgmann C, et al. Isoltrap's multi-reflection time-of-flight mass separator/spectrometer. *Int J Mass Spectrom* (2013) 349-350:123–33. doi:10.1016/j.ijms.2013.03.020

29. Reiter M, Andrés SAS, Bergmann J, Dickel T, Dilling J, Jacobs A, et al. Commissioning and performance of titan's multiple-reflection time-of-flight mass-spectrometer and isobar separator. *Nucl Instrum Methods Phys Res Sect A: Acc* (2021) 1018. 165823. doi:10.1016/j.nima.2021.165823

30. Penttilä H, Beliuskina O, Canete L, de Roubin A, Eronen T, Hukkanen M, et al. Radioactive ion beam manipulation at the igisol-4 facility. *EPJ Web Conf* (2020) 239:17002. doi:10.1051/epjconf/202023917002

31. Okuno H, Dantsuka T, Fujimaki M, Fukunishi N, Hasebe H, Higurashi Y, et al. Present status of and recent developments at riken ri beam factory. *J Phys Conf Ser* (2020) 1401:012005. doi:10.1088/1742-6596/1401/1/012005

32. Wei J, Ao H, Beher S, Bultman N, Casagrande F, Cogan S, et al. Advances of the frib project. *Int J Mod Phys E* (2019) 28:1930003. doi:10.1142/S0218301319300030

33. Wada M, Ishida Y, Nakamura T, Yamazaki Y, Kambara T, Ohyama H, et al. Slow ri-beams from projectile fragment separators. *Nucl Instrum Methods Phys Res B* (2003) 204:570–81. doi:10.1016/s0168-583x(02)02151-1

34. Plaß W, et al. The frs ion catcher - a facility for high-precision experiments with stopped projectile and fission fragments, Nucl. Instrum. Methods Phys. Res. Sect. B: beam Interactions with Materials and Atoms **317**. In: *xVIth international conference on ElectroMagnetic isotope separators and techniques related to their applications, december 2-7, 2012 at matsue, Japan* (2013). p. 457.

35. Villari A, Bollen G, Henriques A, Lapierre A, Nash S, Ringle R, et al. Gas stopping and reacceleration techniques at the facility for rare isotope beams (frib). *Nucl Instrum Methods Phys Res Sect B: Beam Interactions Mater Atoms* (2023) 541:350–4. doi:10.1016/j.nimb.2023.05.037

36. Block M, Ackermann D, Beck D, Blaum K, Breitenfeldt M, Chauduri A, et al. The ion-trap facility shiptrap. *Eur Phys J A - Hadrons Nuclei* (2005) 25:49–50. doi:10.1007/3-540-37642-9_12

37. Ringle R, Bollen G, Prinke A, Savory J, Schury P, Schwarz S, et al. The lebit 9.4t penning trap mass spectrometer. *Nucl Instrum Methods Phys Res Sect A: Acc* (2009) 604:536–47. doi:10.1016/j.nima.2009.03.207

38. Schury P, Wada M, Ito Y, Arai F, Naimi S, Sonoda T, et al. A high-resolution multi-reflection time-of-flight mass spectrograph for precision mass measurements at riken/slowri. *Nucl Instrum Methods Phys Res Sect B* (2014) 335:39–53. doi:10.1016/j.nimb.2014.05.016

39. Rosenbusch M, Wada M, Schury P, Ito Y, Ishiyama H, Ishizawa S, et al. A new multi-reflection time-of-flight mass spectrograph for the slowri facility. *Nucl Instrum Methods Phys Res Sect B* (2020) 463:184–8. doi:10.1016/j.nimb.2019.05.058

40. Kubo T. In-flight RI beam separator bigrips at RIKEN and elsewhere in Japan. *Nucl Instrum Methods Phys Res Sect B* (2003) 204:97–113. doi:10.1016/s0168-583x(02)01896-7

41. Kubo T, Kameda D, Suzuki H, Fukuda N, Takeda H, Yanagisawa Y, et al. Bigrips separator and zerodegree spectrometer at riken ri beam factory. *Prog Theor Exp Phys* (2012) 2012:03C003. doi:10.1093/ptep/pts064

42. Rosenbusch M, Wada M, Chen S, Takamine A, Iimura S, Hou D, et al. The new mrtof mass spectrograph following the zerodegree spectrometer at riken's ribf facility. *Nucl Instrum Methods Phys Res Sect A: Accelerators, Spectrometers, Detectors Associated Equipment* (2023) 1047:167824. doi:10.1016/j.nima.2022.167824

43. Yano Y. The RIKEN RI beam factory project: a status report. *Nucl Instrum Methods Phys Res Sect B* (2007) 261:1009–13. doi:10.1016/j.nimb.2007.04.174

44. Takamine A, et al. Offline test for rf carpet transportation in rf ion guide gas cell at the slowri facility, RIKEN Accel. *Prog Rep* (2019) 52.

45. Liu J, et al. Degrader system for ZD-MRTOF, RIKEN accel. *Prog Rep* (2020) 53:133.

46. Chen S, et al. Degrader optimization for13. ZeroDegree gas cell, RIKEN Accel. *Prog Rep* (2021) 54.

47. Ito Y, Schury P, Wada M, Naimi S, Smorra C, Sonoda T, et al. A novel ion cooling trap for multi-reflection time-of-flight mass spectrograph. *Nucl Instrum Methods Phys Res Sect B* (2013) 317:544–9. doi:10.1016/j.nimb.2013.07.069

48. Ito Y, Schury P, Wada M, Arai F, Haba H, Hirayama Y, et al. First direct mass measurements of nuclides around Z = 100 with a multireflection time-of-flight mass spectrograph. *Phys Rev Lett* (2018) 120:152501. doi:10.1103/physrevlett.120.152501

49. Schury P, Ito Y, Rosenbusch M, Miyatake H, Wada M, Wollnik H. Improving wide-band mass measurements in a multi-reflection time-of-flight mass spectrograph by usage of a concomitant measurement scheme. *Int J Mass Spectrom* (2018) 433:40–6. doi:10.1016/j.ijms.2018.08.007

50. Niwase T, Xian W, Wada M, Rosenbusch M, Chen S, Takamine A, et al. Development of a β-TOF detector: an enhancement of the α-TOF detector for use with β-decaying nuclides. *Prog Theor Exp Phys* (2023) 2023:031H01. doi:10.1093/ptep/ptad039

51. ETP. MagneTOF™: A new class of robust sub-nanosecond tof detectors with exceptional dynamic range. (2013). Available online at: https://www.etp-ms.com/file-repository/8.

52. MCS6A 5(6) input 100ps multi-stop tdc, multiscaler, time-of-flight. (2019). Available online at: https://www.fastcomtec.com/ftp/manuals/mcs6adoc.pdf (Accessed November 13, 2019).

53. Tarasov O, Bazin D. Lise++: radioactive beam production with in-flight separators, nucl. Instrum. Methods phys. Res. Sect. B: beam interactions with materials and atoms 266. In: *Proceedings of the XVth international conference on electromagnetic isotope separators and techniques related to their applications* (2008). p. 4657.

54. Baba H, Ichihara T, Ohnishi T, Takeuchi S, Yoshida K, Watanabe Y, et al. New data acquisition system for the riken radioactive isotope beam factory. *Nucl Instrum Methods Phys Res Sect A: Accelerators, Spectrometers, Detectors Associated Equipment* (2010) 616:65–8. doi:10.1016/j.nima.2010.02.120

55. SpA CAEN, User manual um2792 v1730/vx1730 and v1725/vx1725 (2021).

56. Müller JW. Generalized dead times. *Nucl Instrum Methods Phys Res Sect A: Accelerators, Spectrometers, Detectors Associated Equipment* (1991) 301:543–51. doi:10.1016/0168-9002(91)90021-h

57. Schury P, Wada M, Ito Y, Kaji D, Arai F, MacCormick M, et al. First online multireflection time-of-flight mass measurements of isobar chains produced by fusion-evaporation reactions: toward identification of superheavy elements via mass spectroscopy. *Phys Rev C* (2017) 95:011305. doi:10.1103/physrevc.95.011305

58. Toker Y, Altstein N, Aviv O, Rappaport ML, Heber O, Schwalm D, et al. The kick-out mass selection technique for ions stored in an electrostatic ion beam trap. *J Instrumentation* (2009) 4(09):P09001. doi:10.1088/1748-0221/4/09/p09001

59. Dickel T, Plaß W, Becker A, Czok U, Geissel H, Haettner E, et al. A high-performance multiple-reflection time-of-flight mass spectrometer and isobar separator for the research with exotic nuclei. *Nucl Instrum Methods Phys Res Sect A: Accelerators, Spectrometers, Detectors Associated Equipment* (2015) 777:172–88. doi:10.1016/j.nima.2014.12.094

60. Fischer P, Knauer S, Marx G, Schweikhard L. In-depth study of in-trap high-resolution mass separation by transversal ion ejection from a multi-reflection time-of-flight device. *Rev Scientific Instr* (2018) 89:015114. doi:10.1063/1.5009167

61. APG7400A USB-MCA4 List mode data acquisition, USB bus power. Available online at: https://www.techno-ap.com/img/APG7400A_e.pdf.

62. Kondev F, Wang M, Huang W, Naimi S, Audi G. The NUBASE2020 evaluation of nuclear physics properties. *Chin Phys C* (2021) 45:030001. doi:10.1088/1674-1137/abddae

63. Schury P, Niwase T, Wada M, Morimoto K, Kaji D, Kimura S, et al. Improving energy resolution in an α-TOF detector. *Nucl Phys A* (2025) 1063:123202. doi:10.1016/j.nuclphysa.2025.123202

64. Wang M, Huang W, Kondev F, Audi G, Naimi S. The AME 2020 atomic mass evaluation (II). tables, graphs and references. *Chin Phys C* (2021) 45:030003. doi:10.1088/1674-1137/abddaf

65. Ito Y, Schury P, Wada M, Naimi S, Sonoda T, Mita H, et al. Single-reference high-precision mass measurement with a multireflection time-of-flight mass spectrograph. *Phys Rev C* (2013) 88:011306. doi:10.1103/physrevc.88.011306

66. Xian W, Chen S, Nikas S, Rosenbusch M, Wada M, Ishiyama H, et al. Mass measurements of neutron-rich A ≈ 90 nuclei constrain element abundances. *Phys Rev C* (2024) 109:035804. doi:10.1103/physrevc.109.035804

67. Surman R, Mumpower M, Sinclair R, Jones KL, Hix WR, McLaughlin GC. Sensitivity studies for the weak r process: neutron capture rates. *AIP Adv* (2014) 4:041008. doi:10.1063/1.4867191